nanomaterials

MDPI

Article

Tunable Spin and Orbital Edelstein Effect at (111) $LaAlO_3/SrTiO_3$ Interface

Mattia Trama [1,2,*], Vittorio Cataudella [3,4], Carmine Antonio Perroni [3,4], Francesco Romeo [1] and Roberta Citro [1,2,4]

[1] Physics Department "E.R. Caianiello", Universitá degli Studi di Salerno, I-84084 Fisciano, Italy; fromeo@unisa.it (F.R.); rocitro@unisa.it (R.C.)
[2] INFN—Sezione di Napoli, Complesso Universitá Monte S. Angelo, I-80126 Napoli, Italy
[3] Physics Department "Ettore Pancini", Universitá degli Studi di Napoli "Federico II", Complesso Universitá Monte S. Angelo, I-80126 Napoli, Italy; cataudella@na.infn.it (V.C.); carmine.perroni@unina.it (C.A.P.)
[4] CNR-SPIN Napoli Unit, Complesso Universitá Monte S. Angelo, I-80126 Napoli, Italy
* Correspondence: mtrama@unisa.it

Abstract: Converting charge current into spin current is one of the main mechanisms exploited in spintronics. One prominent example is the Edelstein effect, namely, the generation of a magnetization in response to an external electric field, which can be realized in systems with lack of inversion symmetry. If a system has electrons with an orbital angular momentum character, an orbital magnetization can be generated by the applied electric field, giving rise to the so-called orbital Edelstein effect. Oxide heterostructures are the ideal platform for these effects due to the strong spin–orbit coupling and the lack of inversion symmetries. Beyond a gate-tunable spin Edelstein effect, we predict an orbital Edelstein effect an order of magnitude larger then the spin one at the (111) $LaAlO_3/SrTiO_3$ interface for very low and high fillings. We model the material as a bilayer of t_{2g} orbitals using a tight-binding approach, whereas transport properties are obtained in the Boltzmann approach. We give an effective model at low filling, which explains the non-trivial behaviour of the Edelstein response, showing that the hybridization between the electronic bands crucially impacts the Edelstein susceptibility.

Keywords: Edelstein effect; spin-orbit; orbital magnetization; spintronics; orbitronics; oxide heterostructures

Citation: Trama, M.; Cataudella, V.; Perroni, C.A.; Romeo, F.; Citro, R. Tunable Spin and Orbital Edelstein Effect at (111) $LaAlO_3/SrTiO_3$ Interface. *Nanomaterials* **2022**, *12*, 2494. https://doi.org/10.3390/nano12142494

Academic Editor: Dongchen Qi

Received: 29 June 2022
Accepted: 19 July 2022
Published: 20 July 2022

1. Introduction

Spintronics is an emergent field that exploits the intrinsic spin of the electrons, in addition to its charge. The goal is to produce devices that combine information storage, sensing, and processing in a single platform. In view of their characteristics, these devices could, in principle, overcome the performance of standard electronic devices in terms of data processing speed and consumption [1]. A possibility for spin manipulation is the injection of spin current from ferromagnets to semiconductors, which is, however, inefficient [2].

The best option is provided by the spin-to-charge interconversion, which allows for generating spin current directly inside the materials. In non-magnetic systems, this can be realized, either by the spin Hall effect or the Edelstein effect (EE). The former is the creation of a transverse spin current in response to a charge current [3], whereas the latter is the spin accumulation in response to an applied electric field [4,5]. This spin accumulation can be explained as follows: an electric field $\vec{E}$ shifts the Fermi surfaces of the non-degenerate Kramers doublets, leading to an imbalance of spin and, consequently, a magnetization occurs.

A crucial role in obtaining the EE is the lack of inversion symmetry, which causes a Rashba spin–orbit coupling (SOC), locking the spin with the quasi-momentum of the electrons in a crystal. Oxide heterostructures are therefore the perfect environments for such

a coupling. The interface between the two insulating materials generates a quantum well for the electrons, forming a quasi-two dimensional electronic gas (2DEG), which naturally lays in a system with lack of inversion symmetry [6]. Moreover, in these oxides the atomic SOC is typically stronger than in semiconductor interfaces due to the *d* orbitals of the atom involved in the crystal structure [7]. Therefore, (001) $SrTiO_3$ (STO)-based heterostructures exhibit many non-trivial phenomena based on spin–orbital motion, such as tunable SOC [8], generation and control of spin and orbital textures [9], coexistence of superconductivity and 2D magnetism [7,10], and topological properties both in normal and superconducting states [11–20]. Even if the inverse Edelstein effect, namely, the generation of a charge current in response to a spin current, has been studied more extensively [21], only recently has the EE been taken into account in this system [22,23]. The results are promising, not only due to the presence of the canonical EE, but also because of the presence of the so-called orbital Edelstein effect (OEE) [24], making this interface appealing for the field of orbitronics [25]. Because the electrons of 2DEG have a *d* orbital character, an orbital magnetization occurs in response to an electric field.

The promising results obtained so far with (001) interfaces further motivates the interest into interfaces along other crystallographic directions. The (111) direction has been recently proven to be particularly promising, due to the hexagonal lattice of these structures, which is responsible for many non-trivial phenomena [26–28]. The (111) $LaAlO_3/SrTiO_3$ (LAO/STO) interface has been intensively studied [29–34]. However, there are no predictions or experimental evidence on EE or OEE in this system, even though both the material and the direction are particularly interesting. In this system, the strong orbital intermixing and the peculiar spin and orbital textures [35–37] suggest the possibility of establishing an orbital magnetization and could be of practical interest for the realization of spintronics and orbitronics devices.

Therefore, in this work we theoretically predict the existence of the EE and OEE in the (111) LAO/STO interface, characterizing its properties. We model the material via a bilayer of Ti atoms using three orbital degrees of freedom treated by the tight binding (TB) approach, whereas the transport properties are modeled within the relaxation time approximation of the Boltzmann approach. We predict two different behaviours of the electrical response: a gate-tunable spin EE and an OEE an order of magnitude higher than the spin one, which cannot be explained in a common simplified Rashba model. We show that they emerge from the combined effect of the non-trivial Rashba SOC and the multi-orbital character of the electronic band structure.

2. Methods

The electronic band structure of the LAO/STO interface can be obtained in terms of the t_{2g} orbitals of the Ti atoms in STO [38]. In order to take into account the electronic confinement, we use an accurate TB model, described in Ref. [37], of two layers of Ti atoms projected in the (111) direction, resulting in a honeycomb lattice, as shown in Figure 1. The Hamiltonian we take is

$$H = H_{\mathrm{TB}}(t_D, t_I) + H_{\mathrm{SOC}}(\lambda) + H_{\mathrm{TRI}}(\Delta) + H_v(v), \tag{1}$$

where H_{TB} contains the direct and indirect first neighbour hopping terms, whose amplitude t_D and t_I are fixed in Ref. [36] by fitting the angular resolved photoemission spectroscopy experimental data; H_{SOC} is the atomic spin–orbit coupling of amplitude $\lambda = 0.01$ eV [39], and H_{TRI} is the trigonal crystal field [36] of amplitude $\Delta = -0.005$ eV [40]. Finally, H_v parametrizes the effect of the confinement, which breaks the inversion symmetry and thus generates the so-called orbital Rashba [25], whose amplitude depends on the electric potential v. This term is responsible for the EE. In the region of low filling, a quadratic expansion in the quasimomentum $\vec{k}$ of the Hamiltonian leads to the effective Hamiltonian (the

comparison between the exact microscopic model (1) and the effective Hamiltonian (2) breaks down for $|k| > 0.5$ [37])

$$H_{\text{eff}} = \sum_{i=x,y,z} \mathcal{E}_i(\vec{k})(\mathbb{1} - L_i^2) - \frac{\lambda}{2}\hat{L}\cdot\hat{S} - \frac{3\Delta}{2}L_{111}^2 + \mathcal{F}(\vec{k}\times\hat{L})\cdot\hat{n}_{111} + \varepsilon_0, \tag{2}$$

where $\vec{k}$ is expressed in units of the in-plane lattice constant $\tilde{a} = \sqrt{2/3}a_0 = \sqrt{2/3}\cdot 0.3905$ nm, and $\mathcal{E}_i$ is the renormalized dispersion expanded to second order at $\vec{k}$:

$$\mathcal{E}_x = 0.13k_X^2 - 0.29k_Xk_Y + 0.29k_Y^2, \tag{3}$$

$$\mathcal{E}_y = 0.13k_X^2 + 0.29k_Xk_Y + 0.29k_Y^2, \tag{4}$$

$$\mathcal{E}_z = 0.37k_X^2 + 0.044k_Y^2, \tag{5}$$

where $\mathbb{1}$ is the identity matrix, L_i and S_i are the ith components of the orbital and spin angular momentum operator for $L = 1$ and $S = 1/2$, L_{111} is the projection of the angular momentum along the (111) direction, $\hat{n}_{111}$ is a unitary vector along the (111) direction, the term $\vec{k}\times\hat{L}$ is the orbital Rashba whose strength is included in the coefficient $\mathcal{F} = 0.0035$ eV (depending on v, which is fixed to 0.2 eV), and ε_0 is an energy constant. The expressions and the numerical values of the coefficients in Equation (2) can be found in Appendix A.

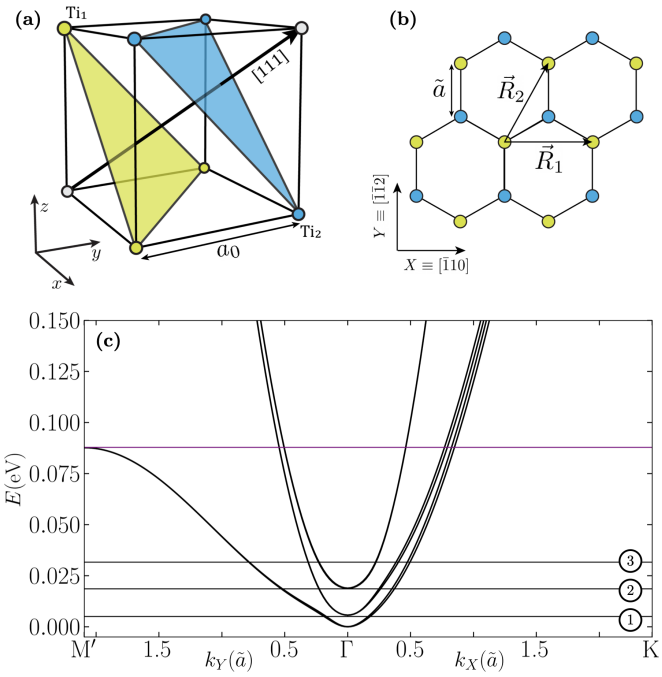

Figure 1. (**a**) Ti atoms in STO lattice, whose lattice constant is $a_0 = 0.3905$ nm. The blue and yellow dots represent atoms belonging to two non-equivalent planes. (**b**) Projection of the two non-equivalent planes of Ti over the (111) plane with our choice of primitive vectors $\vec{R}_1$ and $\vec{R}_2$ and $\tilde{a} = \sqrt{2/3}a_0$. (**c**) Band structure along two different directions in the Brillouin zone. The purple benchmark line corresponds to a Lifshitz transition (see Appendix C).

The combination of the atomic SOC and the orbital Rashba is translated into a generalized total angular momentum Rashba effect of the form $\hat{J}\times\vec{k}$, where $\vec{J}$ is the total angular momentum. The electronic band structure in the low energy region is shown in Figure 1. In the absence of SOC and the trigonal crystal field, all the bands would be degenerate in $\vec{k} = 0$. The splitting between the doublets, due to these couplings, is smaller than in the most studied (001) LAO/STO interface, which is crucial for the results we find. The

vicinity of the bands leads to a strong hybridization, which amplifies the spin and oribital EE. Near Γ, a linear Rashba splitting appears for the lowest Kramers doublet, whereas for the second doublet, a cubic splitting in $\vec{k}$ is found, differing from a simple description of a spin Rashba model [37]. Far away from Γ, the d_{xy}, d_{yz}, d_{zx} character of the bands is restored. The region in which the crossover between these two behaviours occurs is the most sensible to the hybridization of the bands. By fixing the chemical potential to a benchmark value, we observe a non-trivial spin and orbital angular momentum texture on the Fermi surface in Figure 2. First, both the spin and the orbital angular momentum are wrapping around the Fermi contour. The orbital pattern shows that the in-plane component is higher when the Fermi surfaces of two doublets are close to one another, pointing in the same direction, which is a sign of hybridization. The textures for the other benchmark lines are found in Appendix B.

These textures are responsible for the spin and orbital EE when an electric field is included into the system. In linear response theory, the magnetization m_α along the α direction is

$$m_\alpha = \chi_{\alpha\beta} E_\beta, \tag{6}$$

where $\chi_{\alpha\beta}$ is the Edelstein susceptibility, and E_β is the electric field in the β direction; $\chi_{\alpha\beta}$ is the sum of two contributions: a spin contribution $\chi^S_{\alpha\beta}$ and an orbital one $\chi^L_{\alpha\beta}$. We use the Boltzmann approach within the time relaxation approximation to compute the Edelstein susceptibility [22].

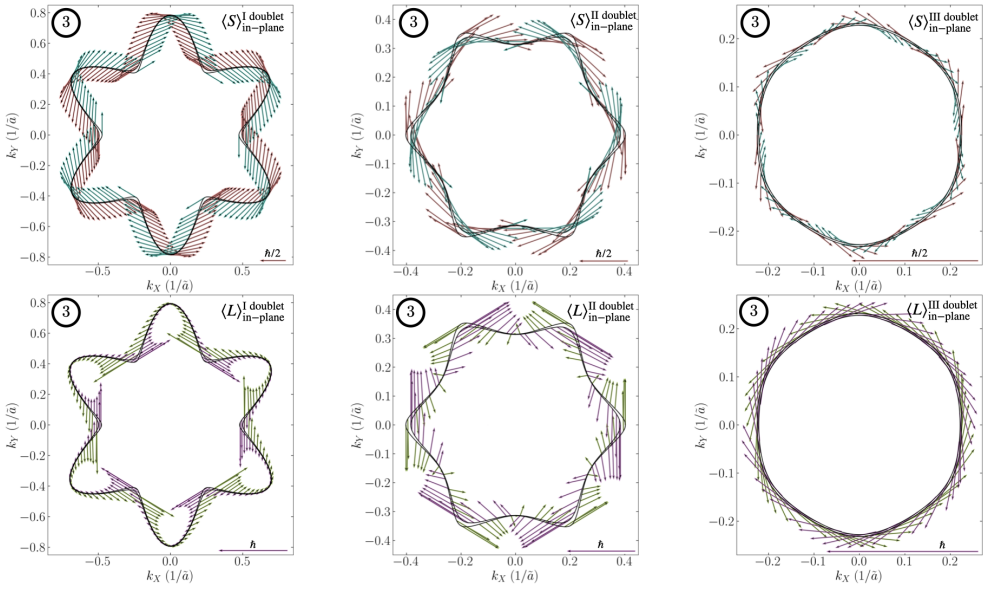

Figure 2. In-plane spin (**upper panel**) and orbital angular momentum (**lower panel**) textures for the three doublets with the chemical potential fixed to the value corresponding to the benchmark line 3 in Figure 1. The red and green arrows represent the mean value of the in-plane component of the operator for the external band, and the blue and purple refer to the internal component. The mean value of the generic operator O is evaluated as $\langle O \rangle = \sqrt{\langle O_{\bar{1}10} \rangle^2 + \langle O_{\bar{1}\bar{1}2} \rangle^2}$.

The magnetic moment per unit cell in the crystal is

$$m_\alpha = \frac{\mu_b}{\hbar} S_{cell} \sum_n \int_{BZ} \frac{d^2\vec{k}}{(2\pi\tilde{a})^2} \ \delta f(\vec{k}) \langle 2S_\alpha + L_\alpha \rangle_n (\vec{k}) \tag{7}$$

where $\langle S_\alpha \rangle_n(\vec{k})$ is the mean value over the eigenstates of the nth band, μ_b is the Bohr magneton, $\hbar$ is the reduced Plank's constant, S_{cell} is the unit cell area, and δf is the modification of the thermal distribution f_{th} in the linear response regime, which is expressed as

$$\delta f(\vec{k}) = -\tau_0 q \tilde{a} \vec{E} \cdot \frac{\partial f_{\text{th}}}{\partial \hbar \vec{k}}. \tag{8}$$

Here τ_0 is the relaxation time, and q is the charge of the electrons. Therefore

$$\chi^{\mathcal{O}}_{\alpha\beta} = \left(-\frac{\tau_0 q \mu_b}{\tilde{a}\hbar^2} S_{cell} \sum_n \int_{BZ} \frac{d^2\vec{k}}{(2\pi)^2} \frac{\partial f_{\text{th}}}{\partial k_\beta} \langle \mathcal{O}_\alpha \rangle_n(\vec{k}) \right), \tag{9}$$

where $\mathcal{O}_\alpha = 2S_\alpha$ or L_α. Due to the anti-symmetric property of the $\chi_{\alpha\beta}$ [41], we need only to evaluate χ_{XY} (with $X = (\bar{1}10)$ and $Y = (\bar{1}\bar{1}2)$ directions). The results are collected in Figure 3 both for the spin and the orbital susceptibility as a function of the chemical potential μ. We fixed the temperature to $T = 10$ K and $\tau_0 = 3.4 \times 10^{-12}$ s, the value of which is derived from the experimental mobility in Ref. [42]. Both susceptibilities behave non-monotonically and they are explicitly decomposed into the contributions of the three Kramers doublets in Equation (9), as also done in [22]. The spin susceptibility changes sign and presents a maximum and a minimum, suggesting that, in real systems, a magnetization reversal can be induced by appropriate gating (e.g., back gate control of the chemical potential).

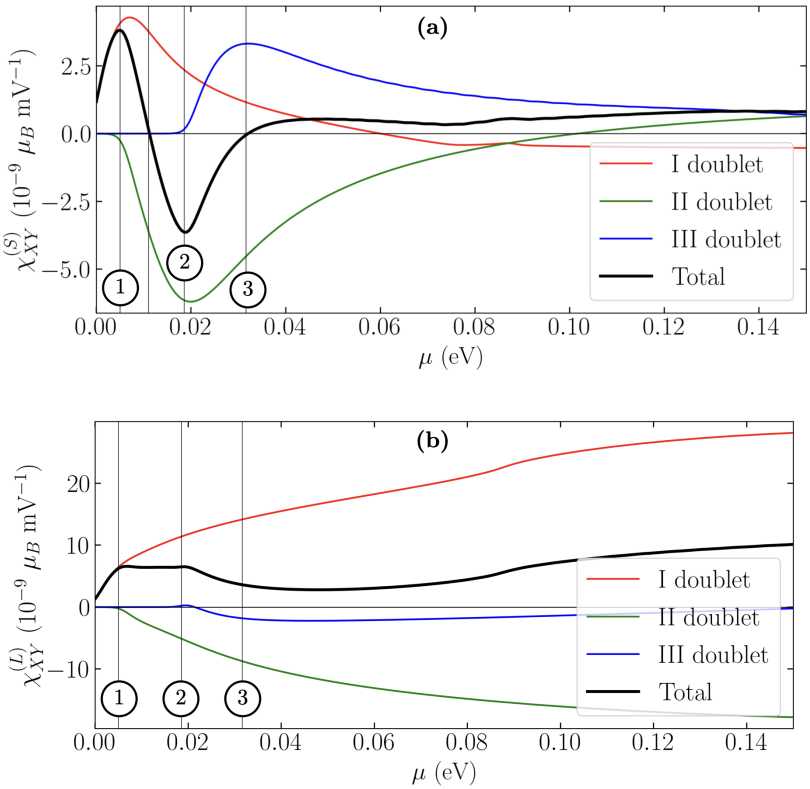

Figure 3. Spin (**a**) and orbital (**b**) Edelstein coefficient as a function of the chemical potential. The different colours correspond to the contribution of a specific Kramers doublet.

In contrast, the orbital susceptibility is always of the order of $10^{-8}\mu_B$ mV^{-1}, which is one order of magnitude greater than the spin susceptibility in the low energy region and above $\mu \sim 0.08$ eV.

We demonstrate that a crucial ingredient for our results is the intermixing between different doublets. The reason is that the orbital Rashba term $\hat{L} \times \vec{k}$ induces an orbital angular

momentum that is larger where the doublets are maximally hybridized. To demonstrate the role of the hybridization, we introduce $P^{\mu} = |\mu\rangle\langle\mu|$ projector along the eigenstate μ of Hamiltonian (1) evaluated for $\vec{k} = 0$. In this case, we identify three different states twice degenerate that we call $|L\sigma\rangle$ (as low), $|M\sigma\rangle$ (as middle), and $|U\sigma\rangle$ (as up). We decompose the spin operator S as

$$S_{\alpha} = \sum_{\mu\nu} P^{\mu} S_{\alpha} P^{\nu} = \sum_{\mu\nu} S_{\alpha}^{\mu\nu}. \tag{10}$$

A similar decomposition is adopted for L. By substituting Equation (10) in Equation (9), one can define an Edelstein susceptibility projected on the states for $\vec{k} = 0$, $\chi_{\alpha\beta}^{\mathcal{O},\mu\nu}$, respecting the condition

$$\chi_{\alpha\beta}^{\mathcal{O}} = \sum_{\mu\nu} \chi_{\alpha\beta}^{\mathcal{O},\mu\nu}. \tag{11}$$

The magnitude of this quantity is an indicator of how much the hybridization of the doublets is important for EE or OEE. The values of $\chi_{XY}^{\mathcal{O},\mu\nu}$ for different benchmark chemical potential are represented in Figure 4. Thus we conclude that, for the first red peak of Figure 3a, there is a strong connection between the first two bands, indicating that this peak is described by a single doublet. However, there is the presence of hybridization with the second doublet as well, which is of the same order of magnitude of the intra-doublet interaction. The effect is even more evident for the angular momentum. By increasing the chemical potential, more doublets are filled, and the hybridization becomes more relevant. However, it is always true that the second intra-doublet contribution is zero, as seen from the 2×2 white square in Figure 4. This is a direct consequence of the absence of linear and quadratic splitting for the two bands in the second doublet. The intermediate doublet mediates the interaction between the first and the third doublet. This is confirmation of the relevance of the multiband model. Differently from the (001) interface, the (111) interface has the three doublets relatively close to one another, leading to this strong orbital hybridization.

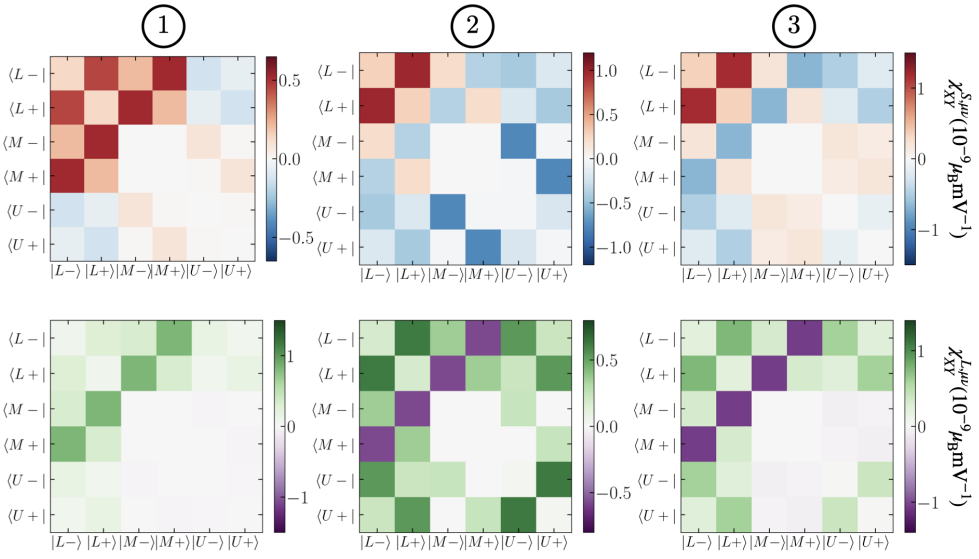

Figure 4. Spin (**upper panel**) and orbital (**lower panel**) Edelstein susceptibility projected over the L, M, and U states. The chemical potential μ is fixed at values 1, 2, and 3, referring to Figure 1.

3. Discussion

We have shown that the multiband character of the (111) LAO/STO is a key feature for the emerging non-linear spin and orbital EE. The strong SOC and the confining potential lead to a non-trivial Rashba interaction. Together with the orbital hybridization of the bands, this allows a spin and orbital magnetic moment in the presence of an in-plane external magnetic field. We have shown through a tight-binding model that the generalized Rashba

effect can generate a non-linear spin EE that changes its sign with the chemical potential and can be modulated with an external gate. Moreover, the strong orbital character of the bands leads to an OEE, an order of magnitude higher than the spin effect at the very low and high fillings. Up to now, there is no direct evidence of orbital magnetization in the experiments. Because one can observe only the full magnetization, it is difficult to disentangle the spin from the orbital response [25]. However, by tuning to zero the spin Edelstein susceptibility, one can disentangle the two components, overcoming this problem. In Appendix C, we show how a $\vec{k}$-dependency on the scattering time changes the results. In principle, the strong orbital degeneracy and the hybridization of the bands could be enhanced by taking into account the contribution by impurities. However, direct computation within the framework of a k-dependent relaxation time shows small quantitative modification of results presented in the main text of this work. In particular, χ^S_{XY} vanishes at the same energy values predicted within the framework of a constant τ theory. Thus, our results provide a consistent picture of the system response. The proposal of tuning the spin response to zero, together with the new proposal of measuring the so-called orbital torque [43], makes the (111) LAO/STO interface suitable for investigating the orbital magnetization and represents a promising spin–orbitronic platform. The orbital angular momentum accumulated through the OEE can be transferred into an adjacent thin ferromagnet. The induced torque is sensitive to the interface crystallinity, and one can realize different experimental setups to capture the angular dependency on the torque. We remark that (111) $KaTiO_3$-based heterostructures [28,44,45] have a similar crystalline structure with higher SOC, which could enhance the EE and OEE. Therefore, they could be an interesting system to further apply our analysis.

Author Contributions: Conceptualization, M.T., R.C.; Formal analysis, M.T.; Investigation, M.T.; Methodology, M.T., V.C., C.A.P., F.R. and R.C.; Project administration, R.C.; Software, M.T.; Supervision, V.C., C.A.P., F.R. and R.C.; Writing—original draft, M.T.; Writing—review & editing, M.T., V.C., C.A.P., F.R. and R.C. All authors have read and agreed to the published version of the manuscript.

Funding: C.A.P. and R.C. acknowledge support from Italy's MIUR PRIN project TOP-SPIN (Grant No. PRIN 20177SL7HC).

Acknowledgments: We acknowledge interesting discussions with M. Bibes.

Conflicts of Interest: The authors declare no conflict of interest.

Abbreviations

The following abbreviations are used in this manuscript:

EE	Edelstein effect
SOC	spin–orbit coupling
2DEG	two-dimensional electronic gas
STO	$SrTiO_3$
LAO	$LaAlO_3$
OEE	orbital Edelstein effect
TB	tight binding

Appendix A. Details of the Model

The effective 2D single-particle Hamiltonian originating from the three t_{2g} orbitals of the Ti-atoms in the bilayer reads [27,36]

$$H = H_{\mathrm{TB}}(t_D, t_I) + H_{\mathrm{SOC}}(\lambda) + H_{\mathrm{TRI}}(\Delta) + H_v(v), \tag{A1}$$

where H_{TB} is the hopping Hamiltonian, which in $\vec{k}$-space can be written as:

$$H_{\mathrm{TB}} = \sum_{\vec{k}} \sum_{i,\alpha\beta,\sigma} t_i^{\alpha\beta}(t_D, t_I, \vec{k}) d^{\dagger}_{i\alpha\sigma,\vec{k}} d_{i\beta\sigma,\vec{k}}, \tag{A2}$$

where $d_{i\alpha\sigma,\vec{k}}$ is the annihilation operator of the electron with 2D dimensionless quasi-momentum $\vec{k} = \tilde{a}\vec{K}$, where $\vec{K}$ is the quasi-momentum, occupying the orbital $i = xy, yz, zx$ belonging to the layer $\alpha, \beta = \mathrm{Ti}_1, \mathrm{Ti}_2$ and of spin $\sigma = \pm 1/2$. The matrix $t_i^{\alpha\beta}(t_D, t_I, \vec{k})$, in the basis $\{d_{yz}, d_{zx}, d_{xy}\} \otimes \{\mathrm{Ti}_1, \mathrm{Ti}_2\}$ is the following:

$$t_i^{\alpha\beta} = \begin{pmatrix} 0 & 0 & 0 & \epsilon_{yz} & 0 & 0 \\ 0 & 0 & 0 & 0 & \epsilon_{zx} & 0 \\ 0 & 0 & 0 & 0 & 0 & \epsilon_{xy} \\ \epsilon_{yz}^* & 0 & 0 & 0 & 0 & 0 \\ 0 & \epsilon_{zx}^* & 0 & 0 & 0 & 0 \\ 0 & 0 & \epsilon_{xy}^* & 0 & 0 & 0 \end{pmatrix}, \tag{A3}$$

where the interlayer contributions are

$$\begin{aligned} \epsilon_{yz} &= -t_D\left(1 + e^{i(\frac{\sqrt{3}}{2}k_X - \frac{3}{2}k_Y)}\right) - t_I e^{-i(\frac{\sqrt{3}}{2}k_X + \frac{3}{2}k_Y)}, \\ \epsilon_{zx} &= -t_D\left(1 + e^{-i(\frac{\sqrt{3}}{2}k_X + \frac{3}{2}k_Y)}\right) - t_I e^{i(\frac{\sqrt{3}}{2}k_X - \frac{3}{2}k_Y)}, \\ \epsilon_{xy} &= -2t_D \cos\left(\frac{\sqrt{3}}{2}k_X\right) e^{-i\frac{3}{2}k_Y} - t_I. \end{aligned} \tag{A4}$$

The direct t_D and indirect t_I couplings have been fixed to the values $t_D = 0.5$ eV and $t_I = 0.04$ eV [36] via comparison with angular resolved photoemission spectroscopy data; H_{SO} is the atomic SOC coupling, which has the following expression:

$$H_{\mathrm{SOC}} = \frac{\lambda}{2}\sum_{\vec{k}}\sum_{ijk,\alpha,\sigma\sigma'} i\varepsilon_{ijk} d^\dagger_{i\alpha\sigma,\vec{k}}\sigma^k_{\sigma\sigma'} d_{j\alpha\sigma',\vec{k}} \tag{A5}$$

where ε_{ijk} is the Levi-Civita tensor, and σ^k are the Pauli matrices. We fix the SOC coupling $\lambda = 0.01$ eV, as a typical order of magnitude [39].

The trigonal crystal field Hamiltonian H_{TRI} takes into account the strain at the interface along the (111) direction. The physical origin of this strain is the possible contraction or dilatation of the crystalline planes along the (111) direction. This coupling has the form [46]

$$H_{\mathrm{TRI}} = \frac{\Delta}{2}\sum_{\vec{k}}\sum_{i\neq j,\alpha,\sigma} d^\dagger_{i\alpha\sigma,\vec{k}} d_{j\alpha\sigma,\vec{k}}. \tag{A6}$$

We fix $\Delta = -0.005$ eV, as reported in [40].

Finally, the last term H_v describes an electric field in the (111) direction, orthogonal to the interface, which breaks the reflection symmetry. The Hamiltonian H_v can thus be written as the sum of an electrostatic potential H_{v0} and a term that induces the breaking of the inversion symmetry in the orbitals H_{BIS}:

$$H_v = \frac{v}{2}\sum_{i,\alpha,\sigma,\vec{k}} \xi_\alpha d^\dagger_{i\alpha\sigma,\vec{k}} d_{i\alpha\sigma,\vec{k}} + \sum_{\vec{k}}\sum_{ij,\alpha\beta,\sigma} h^{\alpha\beta}_{ij,\vec{k}}(v) d^\dagger_{i\alpha\sigma,\vec{k}} d_{j\beta\sigma,\vec{k}} = H_{v0} + H_{\mathrm{BIS}}, \tag{A7}$$

where $\xi_{\mathrm{Ti}_1/\mathrm{Ti}_2} = \pm 1$. For ease of writing, $h^{\alpha\beta}_{ij,\vec{k}}(v)$ is written as the sum of two components: an interlayer contribution, connecting the two layers Ti_1 and Ti_2, as

$$h^{\mathrm{Ti}_1\mathrm{Ti}_2}_{ij,\vec{k}} = h^{\mathrm{Ti}_2\mathrm{Ti}_1}_{ij,\vec{k}} = \eta_p \frac{V_{pd\pi}(\sqrt{2})^{7/4}}{\sqrt{15}} \begin{pmatrix} 0 & -2ie^{i\frac{3}{2}k_Y}\sin\left(\frac{\sqrt{3}}{2}k_X\right) & 1 - e^{\frac{i}{2}(\sqrt{3}k_X + 3k_Y)} \\ 2ie^{i3/2k_Y}\sin\left(\frac{\sqrt{3}}{2}k_X\right) & 0 & 1 - e^{-\frac{i}{2}(\sqrt{3}k_X - 3k_Y)} \\ -1 + e^{\frac{i}{2}(\sqrt{3}k_X + 3k_Y)} & -1 + e^{-\frac{i}{2}(\sqrt{3}k_X - 3k_Y)} & 0 \end{pmatrix}, \tag{A8}$$

and an interlayer contribution as $h^{\mathrm{Ti_1Ti_1}}_{ij,\vec{k}} = h^{\mathrm{Ti_2Ti_2}}_{ij,\vec{k}} = h^{\pi}_{ij,\vec{k}} + h^{\sigma}_{ij,\vec{k}}$ where

$$h^{\pi}_{ij,\vec{k}} = \eta_p \frac{2i}{\sqrt{15}} V_{pd\pi} \begin{pmatrix} 0 & -(\sin(\kappa_1)+\sin(\kappa_2)+2\sin(\kappa_3)) & (\sin(\kappa_1)+2\sin(\kappa_2)+\sin(\kappa_3)) \\ (\sin(\kappa_1)+\sin(\kappa_2)+2\sin(\kappa_3)) & 0 & -(2\sin(\kappa_1)+\sin(\kappa_2)+\sin(\kappa_3)) \\ (\sin(\kappa_1)+2\sin(\kappa_2)+\sin(\kappa_3)) & (2\sin(\kappa_1)+\sin(\kappa_2)+\sin(\kappa_3)) & 0 \end{pmatrix}, \tag{A9}$$

$$h^{\sigma}_{ij,\vec{k}} = \eta_p \frac{2i}{\sqrt{15}} \sqrt{3} V_{pd\sigma} \begin{pmatrix} 0 & (\sin(\kappa_1)+\sin(\kappa_2)) & -(\sin(\kappa_1)+\sin(\kappa_3)) \\ -(\sin(\kappa_1)+\sin(\kappa_2)) & 0 & (\sin(\kappa_2)+\sin(\kappa_3)) \\ (\sin(\kappa_1)+\sin(\kappa_3)) & -(\sin(\kappa_2)+\sin(\kappa_3)) & 0 \end{pmatrix}, \tag{A10}$$

with $\kappa_1 = -\frac{\sqrt{3}}{2}k_X + \frac{3}{2}k_Y$, $\kappa_2 = -\frac{\sqrt{3}}{2}k_X - \frac{3}{2}k_Y$, $\kappa_3 = \sqrt{3}k_X$, $V_{pd\pi} = 0.028$ eV and $V_{pd\sigma} = -0.065$ eV, $\eta_p \sim \frac{v\sqrt{3}}{a_0}\frac{1}{10\,\mathrm{eV/nm}} \sim 0.09$ by using $v = 0.2$ eV and $a_0 = 3.905$ nm. The electric field has been fixed at the value $v = 0.2$ eV by comparison with the Rashba splitting evaluated in Ref. [39]. The full derivation of Equation (A7) can be found in the Supplementary Material of Ref. [37].

Appendix A.1. Expansion at Low Fillings

The whole matrix $H_{\mathrm{TB}} + H_{v0}$, which is 12×12, admits as eigenstates

$$\left|\psi_{i\sigma,\vec{k}}\pm\right\rangle = \alpha_i(\vec{k})e^{i\phi_i(\vec{k})}\left|d_{i1\sigma,k}\right\rangle + \beta_i^{\pm}(\vec{k})\left|d_{i2\sigma,k}\right\rangle, \tag{A11}$$

with

$$\begin{aligned} \alpha_i^{\pm}(\vec{k}) &= \frac{|\epsilon_i(\vec{k})|}{\sqrt{2|\epsilon_i(\vec{k})|^2 + \frac{v^2}{2} \pm v\sqrt{\frac{v^2}{4} + |\epsilon_i(\vec{k})|^2}}}; \\ \beta_i^{\pm}(\vec{k}) &= \frac{\left(\frac{v}{2} \pm \sqrt{\frac{v^2}{4} + |\epsilon_i(\vec{k})|^2}\right)}{\sqrt{2|\epsilon_i(\vec{k})|^2 + \frac{v^2}{2} \pm v\sqrt{\frac{v^2}{4} + |\epsilon_i(\vec{k})|^2}}}; \\ \phi_i(\vec{k}) &= \arg[\epsilon_i(\vec{k})] \end{aligned} \tag{A12}$$

where the orbitals are labeled by the index i and the spin using the index σ. The corresponding eigenvalues are

$$\rho_i^{\pm}(\vec{k}) = \pm\sqrt{\frac{v^2}{4} + |\epsilon_i(\vec{k})|^2}, \tag{A13}$$

which expanded at the second order in $\vec{k}$ gives the expression $\mathcal{E}_i$ of Equations (3)–(5) in the main text.

In order to obtain the orbital Rashba Hamiltonian on the six lower bands for low fillings, we simultaneously linearize the electric field Hamiltonian H_{BIS} of Equation (A7) as a function of $\vec{k}$ and evaluate its matrix elements among the six lower states in Equation (A11), evaluated for $\vec{k} = 0$. The result is the following linear Hamiltonian:

$$(H_{\mathrm{BIS}})_{ij} = -i\mathcal{F}\varepsilon_{ijk}\kappa_k, \quad \text{where} \quad \mathcal{F} = \frac{2\eta_p}{\sqrt{15}}\left(V_{pd\pi}(1 + 2^{7/8}\alpha\beta\cos(\phi)) + \sqrt{3}V_{pd\sigma}\right), \tag{A14}$$

$\vec{\kappa} = (\kappa_1, \kappa_2, \kappa_3)$ as defined above and α, β, and ϕ are the Equations (A12) evaluated for $\vec{k} = 0$.

Identifying now the matrix elements of the orbital angular momentum $\hat{L}$ matrices, we can rewrite this term as:

$$H_{\mathrm{BIS}} = \frac{3}{\sqrt{2}}\mathcal{F}(\vec{k} \times \hat{L}) \cdot \hat{n}_{111}, \tag{A15}$$

where $\hat{n}_{111}$ is a unitary vector along the (111) direction.

Having introduced the notation of the angular momentum, we can also write the TB over the states (A11) using the same notation:

$$H_{\mathrm{TB}} = \sum_i \mathcal{E}_i(\mathbb{1} - L_i^2) \otimes \mathbb{1}_{\sigma\sigma'}. \tag{A16}$$

In addition, H_{TRI} can be expressed in the form

$$H_{\mathrm{TRI}} = \Delta(\mathbb{1} - \frac{3}{2}L_{111}^2). \tag{A17}$$

Appendix B. Spin and Orbital Textures

In Figure A1, we report the spin and orbital angular momentum textures for the benchmark lines 1 and 2 of Figure 1. For the benchmark line 1, the spin and the angular momentum follow the same pattern, which reflects the dominance of the atomic SOC in this region: the total angular momentum $\hat{J}$ is the conserved quantity and therefore both $\langle \hat{L} \rangle$ and $\langle \hat{S} \rangle$ are proportional to $\langle \hat{J} \rangle$. For the benchmark line 2, a second doublet is occupied, and the hybridization of the bands is present. In this case, the patterns for the spin and the orbital angular momentum are different. The in-plane $\langle \hat{L} \rangle$ is higher where the bands are maximally hybridized.

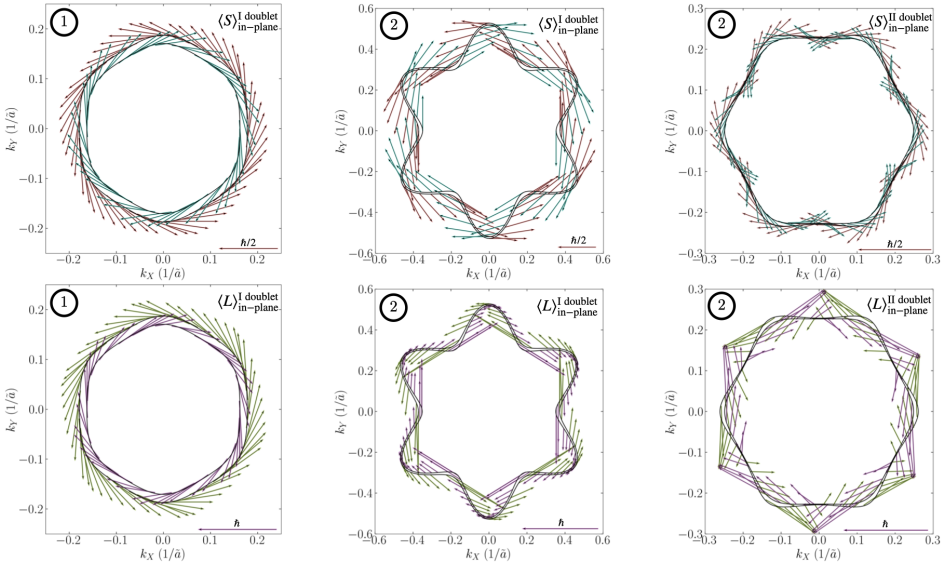

Figure A1. In-plane spin (**upper panel**) and orbital angular momentum (**lower panel**) textures for the first and the second doublet with the chemical potential fixed to the value corresponding to the benchmark lines 1 and 2 in Figure 1. The red and green arrows represent the mean value of the in-plane component of the operator for the external band, and the blue and pink refer to the internal component. The mean value of the generic operator O is evaluated as $\langle O \rangle = \sqrt{\langle O_{\bar{1}10} \rangle^2 + \langle O_{\bar{1}12} \rangle^2}$.

Appendix C. Role of Impurities Scattering on the Edelstein Effect

In the main text, we assumed τ to be independent of the quasi-momentum, following the assumptions of the previous work in Ref. [22]. In this section, we show the prediction for the Edelstein susceptibility when the dependence of the scattering time τ on $\vec{k}$ is included. We consider a point-like impurity, e.g., oxygen vacancy, a kind of defect typical of $SrTiO_3$ heterostructures [47–49].

The unperturbed Hamiltonian is

$$H_{\vec{k}} = \sum_{\alpha\beta\vec{k}} h_{\alpha\beta\vec{k}} c^\dagger_{\alpha\vec{k}} c_{\beta\vec{k}} = \sum_{a\vec{k}} \epsilon_{a\vec{k}} c^\dagger_{a\vec{k}} c_{a\vec{k}}, \tag{A18}$$

where the Greek indices label the orbital degrees of freedom, whereas the Latin ones label the diagonalized bands. The change of basis due to the diagonalization is ruled by the following transformation:

$$c_{a\vec{k}} = U^{\vec{k}}_{a,\alpha} c_{\alpha\vec{k}}. \tag{A19}$$

An impurity can occupy the position of an atom in the lattice. Because the elementary cell contains two atoms (Ti_1 or Ti_2), we will distinguish the degrees of freedom as $\alpha = o, t$, where t labels the kind of atom in the unit cell, and o labels all the other degrees of freedom (spin and orbitals).

With the previous definitions, we write the impurity Hamiltonian of N impurities that can randomly occupy an atom position as

$$H_{\mathrm{I}} = \sum_{i,oo'} \frac{\epsilon^I_{oo'}}{v} c^\dagger_{ot_i,r_i} c_{o't_i,r_i} = \sum_{\vec{k}\,\vec{q}} \sum_{i,oo'} \frac{\epsilon^I_{oo'}}{v} c^\dagger_{ot_i\vec{k}} c_{o't_i\vec{q}} e^{i\frac{(\vec{q}-\vec{k})}{\hbar}\cdot\vec{r}_i} = \sum_{\vec{k}\,\vec{q}} \sum_{i,ab} \frac{\varepsilon^{\vec{k}\vec{q}}_{ab,t_i}}{v} c^\dagger_{a\vec{k}} c_{b\vec{q}} e^{i\frac{(\vec{q}-\vec{k})}{\hbar}\cdot\vec{r}_i}, \tag{A20}$$

where we summed over all the impurities i in the first sum, defined v the volume of the crystal, $\epsilon^I_{oo'} = \int d^3\vec{r}\; V_{oo'}(\vec{r}-\vec{r}_i)$, $V_{oo'}(\vec{r}-\vec{r}_i)$ the impurity potential, $\vec{r}_i$ the position of the impurity, and $\varepsilon^{\vec{k}\vec{q}}_{ab,t_i} = \sum_{oo'} \epsilon^I_{oo'} U^{\vec{k}}_{a,ot_i} U^{\vec{p}\dagger}_{b,o't_i}$. We do not sum over the label t_i because every impurity occupies only one layer. We take the following form for the impurity energy tensor:

$$\epsilon^I_{oo'} = \epsilon_0 \delta_{oo'}. \tag{A21}$$

This expression is the simplest coupling for the scattering; the electron maintains its spin and orbital character, preserving the symmetries of the system. This choice allows us to have control on the results and see the differences with respect to the constant τ. With such a definition, we can perform a diagrammatic calculation for evaluating the self-energy due to the impurities. We perform an average over all the positions r_i and all the layer occupation t_i, which are independent distributions. The imaginary part of the self-energy for the ath band located at the t layer, up to the second order of perturbation theory over the strength of the impurity potential, is

$$\mathrm{Im}(\Sigma^a_{t,\vec{k}}) = -\frac{\hbar}{2\tau^a_{\vec{k}}} = -n_i \frac{\varepsilon_0^2}{v} \pi \sum_{\vec{p}} \sum_b \delta(\hbar\omega^a_{\vec{k}} - \hbar\omega^b_{\vec{p}}) \Big| \sum_{oo'} U^{\vec{k}}_{a,ot} U^{\vec{p}\dagger}_{b,ot} \Big|^2, \tag{A22}$$

where n_i is the impurity density. This coincides with the inverse of the scattering time and is shown in Figure A2 as a function of the chemical potential μ (or $\hbar\omega^a_{\vec{k}}$) for some benchmark directions in the BZ. The averaged $1/\tau^a_{\vec{k}}$ over the t layers is therefore

$$\frac{1}{\tau^a_{\vec{k}}} = \left(\frac{1}{\tau^a_{\mathrm{Ti}_1\vec{k}}} + \frac{1}{\tau^a_{\mathrm{Ti}_2\vec{k}}} \right) \frac{1}{2}. \tag{A23}$$

The magnitude of the coupling ϵ_0 is determined by averaging $\tau_{\vec{k}}$ over the whole BZ and fixing the mean value at the experimental value τ_0 [42] used in the main text. With such a scattering time, the Edelstein response is

$$\chi^{\mathcal{O}}_{\alpha\beta} = -\frac{q\mu_b}{\tilde{a}\hbar^2} S_{cell} \sum_n \int_{BZ} \frac{d^2\vec{k}}{(2\pi)^2} \frac{\partial f_{th}}{\partial k_\beta} \tau_n(\vec{k}) \langle \mathcal{O}_\alpha \rangle_n(\vec{k}). \tag{A24}$$

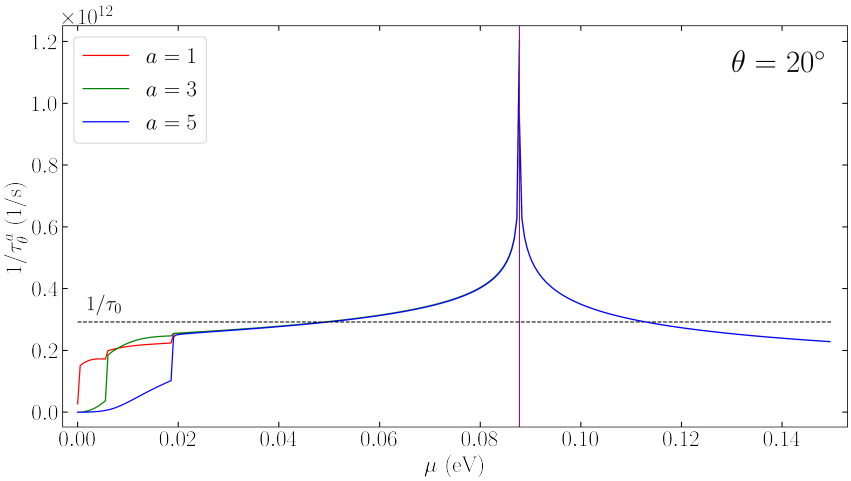

Figure A2. Graph of $1/\tau$ as a function of the chemical potential for a benchmark direction in the Brillouin zone. The dashed line corresponds to the inverse of the scattering time used in the main text. The purple vertical line corresponds to the energy at which a Lifshitz transition occurs for first band (see Figure A3).

The results obtained using a temperature of $T = 10$ K are shown in Figure A3.

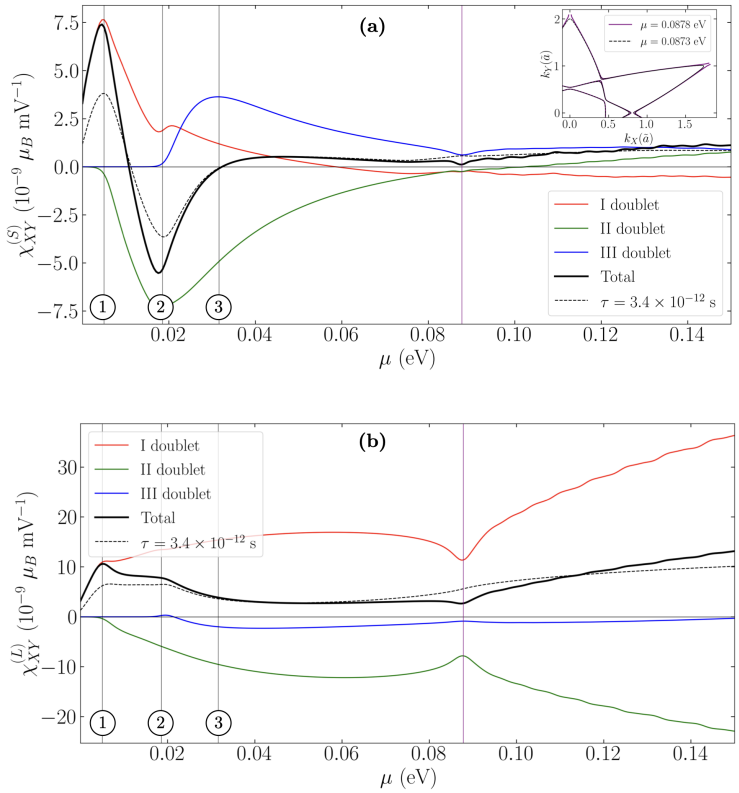

Figure A3. Spin (**a**) and orbital (**b**) Edelstein coefficient as a function of the chemical potential using a scattering time model with a point-like impurity. The different colours correspond to the contribution of a specific Kramers doublet, whereas the dashed line corresponds to the total Edelstein response for a constant τ. The inset in panel (**a**) corresponds to the detail of the Fermi energy contour for the purple chemical potential line.

Here we can see that impurities do not substantially modify the behaviour of the curves, but change the response quantitatively, especially for low fillings. We notice the appearance of local minima at the second benchmark chemical potential for the first doublet and a drop of the response at the purple vertical line. In both cases, the susceptibility has a drop due to the large number of states available for the scattering, which reduce the scattering lifetime and, consequently, the Edelstein response. In the first case, the maximal mixing between the bands induces the appearance of the local minima, as shown in Figure 4, whereas in the second case, the drop is due to the Lifshtiz transition for the first doublet, as shown in Figure A3.

References

1. Dieny, B.; Prejbeanu, I.L.; Garello, K.; Gambardella, P.; Freitas, P.; Lehndorff, R.; Raberg, W.; Ebels, U.; Demokritov, S.O.; Akerman, J.; et al. Opportunities and challenges for spintronics in the microelectronics industry. *Nat. Electron.* **2020**, *3*, 446–459. [CrossRef]
2. Wolf, S.A.; Awschalom, D.D.; Buhrman, R.A.; Daughton, J.M.; Molnár, V.V.; Roukes, M.L.; Chtchelkanova, A.Y.; Treger, D.M. Spintronics: A spin-based electronics vision for the future. *Science* **2001**, *294*, 1488–1495. [CrossRef] [PubMed]
3. Dyakonov, M.I.; Perel, V.I. Current-induced spin orientation of electrons in semiconductors. *Phys. Lett. A* **1971**, *35*, 459–460. [CrossRef]
4. Edelstein, V.M. Spin polarization of conduction electrons induced by electric current in two-dimensional asymmetric electron systems. *Solid State Commun.* **1990**, *73*, 233–235. [CrossRef]
5. Aronov, A.G.; Lyanda-Geller, Y.B. Nuclear electric resonance and orientation of carrier spins by an electric field. *Sov. Phys. JETP* **1989**, *50*, 431.
6. Lin, W.; Li, L.; Doğan, F.; Li, C.; Rotella, H.; Yu, X.; Zhang, B.; Li, Y.; Lew, W.S.; Wang, S.; et al. Interface-based tuning of rashba spin-orbit interaction in asymmetric oxide heterostructures with 3d electrons. *Nat. Commun.* **2019**, *10*, 3052. [CrossRef] [PubMed]
7. Hwang, H.Y.; Iwasa, Y.; Kawasaki, M.; Keimer, B.; Nagaosa, N.; Tokura, Y. Emergent phenomena at oxide interfaces. *Nat. Mater.* **2012**, *11*, 103–113. [CrossRef]
8. Caviglia, A.D.; Gabay, M.; Gariglio, S.; Reyren, N.; Cancellieri, C.; ; Triscone, J.-M. Tunable rashba spin-orbit interaction at oxide interfaces. *Phys. Rev. Lett.* **2010**, *104*, 126803. [CrossRef]
9. Gariglio, S.; Caviglia, A.D.; Triscone, J.; Gabay, M. A spin–orbit playground: Surfaces and interfaces of transition metal oxides. *Rep. Prog. Phys.* **2018**, *82*, 012501. [CrossRef]
10. Pai, Yu.; Tylan-Tyler, A.; Irvin, P.; Levy, J. Physics of $SrTiO_3$-based heterostructures and nanostructures: A review. *Rep. Prog. Phys.* **2018**, *81*, 036503. [CrossRef]
11. Vivek, M.O.G.M.; Gabay, M. Topological states at the (001) surface of $SrTiO_3$. *Phys. Rev. B* **2017**, *95*, 165117. [CrossRef]
12. Scheurer, M.S.; Schmalian, J. Topological superconductivity and unconventional pairing in oxide interfaces. *Nat. Commun.* **2015**, *6*, 6005. [CrossRef] [PubMed]
13. Mohanta, N.; Taraphder, A. Topological superconductivity and Majorana bound states at the $LaAlO_3/SrTiO_3$ interface. *EPL* **2014**, *108*, 60001. [CrossRef]
14. Loder, F.; Kampf, A.P.; Kopp, T. Route to topological superconductivity via magnetic field rotation. *Sci. Rep.* **2015**, *5*, 15302. [CrossRef] [PubMed]
15. Fukaya, Y.; Tamura, S.; Yada, K.; Tanaka, Y.; Gentile, P.; Cuoco, M. Interorbital topological superconductivity in spin-orbit coupled superconductors with inversion symmetry breaking. *Phys. Rev. B* **2018**, *97*, 174522. [CrossRef]
16. Fidkowski, L.; Lutchyn, R.M.; Nayak, C.; Fisher, M.P.A. Majorana zero modes in one-dimensional quantum wires without long-ranged superconducting order. *Phys. Rev. B* **2011**, *84*, 195436. [CrossRef]
17. Fidkowski, L.; Jiang, H.; Lutchyn, R.M.; Nayak, C. Magnetic and superconducting ordering in one-dimensional nanostructures at the $LaAlO_3/SrTiO_3$ interface. *Phys. Rev. B* **2013**, *87*, 014436. [CrossRef]
18. Mazziotti, M.V.; Scopigno, N.; Grilli, M.; Caprara, S. Majorana Fermions in One-Dimensional Structures at $LaAlO_3/SrTiO_3$ Oxide Interfaces. *Condens. Matter* **2018**, *3*, 37. [CrossRef]
19. Perroni, C.A.; Cataudella, V.; Salluzzo, M.; Cuoco, M.; Citro, R. Evolution of topological superconductivity by orbital-selective confinement in oxide nanowires. *Phys. Rev. B* **2019**, *100*, 094526. [CrossRef]
20. Settino, J.; Forte, F.; Perroni, C.A.; Cataudella, V.; Cuoco, M.; Citro, R. Spin-orbital polarization of majorana edge states in oxide nanowires. *Phys. Rev. B* **2020**, *102*, 224508. [CrossRef]
21. Trier, F.; Vaz, D.C.; Bruneel, P.; Noël, P.; Fert, A.; Vila, L.; Attané, J.; Barthélémy, A.; Gabay, M.; Jaffrès, H.; et al. Electric-field control of spin current generation and detection in ferromagnet-free $SrTiO_3$-based nanodevices. *Nano Lett.* **2019**, *20*, 395–401. [CrossRef] [PubMed]
22. Johansson, A.; Göbel, B.; Henk, J.; Bibes, M.; Mertig, I. Spin and orbital edelstein effects in a two-dimensional electron gas: Theory and application to $SrTiO_3$ interfaces. *Phys. Rev. Res.* **2021**, *3*, 013275. [CrossRef]
23. Chirolli, L.; Mercaldo, M.T.; Guarcello, C.; Giazotto, F.; Cuoco, M. Colossal orbital edelstein effect in noncentrosymmetric superconductors. *Phys. Rev. Lett.* **2022**, *128*, 217703. [CrossRef] [PubMed]

24. Levitov, L.S.; Nazarov, Y.V.; Eliashberg, G.M. Magnetoelectric effects in conductors with mirror isomer symmetry. *Sov. Phys. JETP* **1985**, *61*, 133.
25. Go, D.; Jo, D.; Lee, H.; Kläui, M.; Mokrousov, Y. Orbitronics: Orbital currents in solids. *EPL* **2021**, *135*, 37001. [CrossRef]
26. Chakhalian, J.; Liu, X.; Fiete, G.A. Strongly correlated and topological states in [111] grown transition metal oxide thin films and heterostructures. *APL Mater.* **2020**, *8*, 050904. [CrossRef]
27. Xiao, D.; Zhu, W.; Ran, Y.; Nagaosa, N.; Okamoto, S. Interface engineering of quantum hall effects in digital transition metal oxide heterostructures. *Nat. Commun.* **2011**, *2*, 596. [CrossRef]
28. Bruno, F.Y.; Walker, S.M.; Riccò, S.; Torre, A.D.L.; Wang, Z.; Tamai, A.; Kim, T.K.; Hoesch, M.; Bahramy, M.S.; Baumberger, F. Band structure and spin–orbital texture of the (111)-ktao3 2d electron gas. *Adv. Electron. Mater.* **2019**, *5*, 1800860. [CrossRef]
29. Boudjada, N.; Wachtel, G.; Paramekanti, A. Magnetic and nematic orders of the two-dimensional electron gas at oxide (111) surfaces and interfaces. *Phys. Rev. Lett.* **2018**, *120*, 086802. [CrossRef]
30. Rout, P.K.; Agireen, I.; Maniv, E.; Goldstein, M.; Dagan, Y. Six-fold crystalline anisotropic magnetoresistance in the (111) $LaAlO_3/SrTiO_3$ oxide interface. *Phys. Rev. B* **2017**, *95*, 241107. [CrossRef]
31. Monteiro, A.M.R.V.L.; Groenendijk, D.J.; Groen, I.; de Bruijckere, J.; Gaudenzi, R.; Zant, H.S.J.V.D.; Caviglia, A.D. Two-dimensional superconductivity at the (111) $LaAlO_3/SrTiO_3$ interface. *Phys. Rev. B* **2017**, *96*, 020504. [CrossRef]
32. Davis, S.; Huang, Z.; Han, K.; Venkatesan, T.; Chandrasekhar, V. Magnetoresistance in the superconducting state at the (111) $LaAlO_3/SrTiO_3$ interface. *Phys. Rev. B* **2017**, *96*, 134502. [CrossRef]
33. Doennig, D.; Pickett, W.E.; Pentcheva, R. Massive Symmetry Breaking in $LaAlO_3/SrTiO_3$ (111) Quantum Wells: A Three-Orbital Strongly Correlated Generalization of Graphene. *Phys. Rev. Lett.* **2013**, *111*, 126804. [CrossRef] [PubMed]
34. Khanna, U.; Rout, P.K.; Mograbi, M.; Tuvia, G.; Leermakers, I.; Zeitler, U.; Dagan, Y.; Goldstein, M. Symmetry and Correlation Effects on Band Structure Explain the Anomalous Transport Properties of (111) $LaAlO_3/SrTiO_3$. *Phys. Rev. Lett.* **2019**, *123*, 036805. [CrossRef] [PubMed]
35. He, P.; Walker, S.M.; Zhang, S.S.; Bruno, F.Y.; Bahramy, M.S.; Lee, J.M.; Ramaswamy, R.; Cai, K.; Heinonen, O.; Vignale, G.; et al. Observation of out-of-plane spin texture in a $SrTiO_3$ (111) two-dimensional electron gas. *Phys. Rev. Lett.* **2018**, *120*, 266802. [CrossRef]
36. Trama, M.; Cataudella, V.; Perroni, C.A. Strain-induced topological phase transition at (111) $SrTiO_3$-based heterostructures. *Phys. Rev. Res.* **2021**, *3*, 043038. [CrossRef]
37. Trama, M.; Perroni, C.A.; Cataudella, V.; Romeo, F.; Citro, R. Gate tunable anomalous Hall effect at (111) $LaAlO_3/SrTiO_3$ interface. *arXiv* **2022**, arXiv:2202.04664.
38. Keppler, H. *Crystal Field Theory*; Springer: Dordrecht, The Netherlands, 1998; pp. 118–120.
39. Monteiro, A.M.R.V.L.; Vivek, M.; Groenendijk, D.J.; Bruneel, P.; Leermakers, I.; Zeitler, U.; Gabay, M.; Caviglia, A.D. Band inversion driven by electronic correlations at the (111) $LaAlO_3/SrTiO_3$ interface. *Phys. Rev. B* **2019**, *99*, 201102. [CrossRef]
40. Luca, G.M.D.; Capua, R.D.; Gennaro, E.D.; Sambri, A.; Granozio, F.M.; Ghiringhelli, G.; Betto, D.; Piamonteze, C.; Brookes, N.B.; Salluzzo, M. Symmetry breaking at the (111) interfaces of $SrTiO_3$ hosting a two-dimensional electron system. *Phys. Rev. B* **2018**, *98*, 115143. [CrossRef]
41. Shen, K.; Vignale, G.; Raimondi, R. Microscopic theory of the inverse edelstein effect. *Phys. Rev. Lett.* **2014**, *112*, 096601. [CrossRef]
42. Khan, T.; Zhang, H.; Zhang, H.; Yan, X.; Hong, D.; Han, F.; Chen, Y.; Shen, B.; Sun, J. High mobility 2-dimensional electron gas at $LaAlO_3/SrTiO_3$ interface prepared by spin coating chemical methods. *Nanotechnology* **2017**, *28*, 435701. [CrossRef] [PubMed]
43. Bhowal, S.; Vignale, G. Orbital hall effect as an alternative to valley hall effect in gapped graphene. *Phys. Rev. B* **2021**, *103*, 195309. [CrossRef]
44. Bareille, C.; Fortuna, F.; Rödel, T.C.; Bertran, F.; Gabay, M.; Cubelos, O.H.; Taleb-Ibrahimi, A.; Fevre, P.L.; Bibes, M.; Barthélémy, A.; et al. Two-dimensional electron gas with six-fold symmetry at the (111) surface of $KTaO_3$. *Sci. Rep.* **2014**, *4*, 3586. [CrossRef] [PubMed]
45. Vicente-Arche, L.M.; Bréhin, J.; Varotto, S.; Cosset-Cheneau, M.; Mallik, S.; Salazar, R.; Noël, P.; Vaz, D.C.; Trier, F.; Bhattacharya, S.; et al. Spin–charge interconversion in $KTaO_3$ 2D electron gases. *Adv. Mater.* **2021**, *33*, 2102102. [CrossRef]
46. Khomskii, D. *Transition Metal Compounds*; Cambridge University Press: Cambridge, UK, 2014.
47. Kalabukhov, A.; Gunnarsson, R.; Börjesson, J.; Olsson, E.; Claeson, T.; Winkler, D. Effect of oxygen vacancies in the $SrTiO_3$ substrate on the electrical properties of the $LaAlO_3$/ $SrTiO_3$ interface. *Phys. Rev. B* **2007**, *75*, 121404. [CrossRef]
48. Li, Y.; Phattalung, S.N.; Limpijumnong, S.; Kim, J.; Yu, J. Formation of oxygen vacancies and charge carriers induced in the n-type interface of a $LaAlO_3$ overlayer on $SrTiO_3$ (001). *Phys. Rev. B* **2011**, *84*, 245307. [CrossRef]
49. Walker, S.M.; Torre, A.D.L.; Bruno, F.Y.; Tamai, A.; Kim, T.K.; Hoesch, M.; Shi, M.; Bahramy, M.S.; King, P.D.C.; Baumberger, F. Control of a two-dimensional electron gas on $SrTiO_3$ (111) by atomic oxygen. *Phys. Rev. Lett.* **2014**, *113*, 177601. [CrossRef]